Fourth International Symposium on Marine Propulsors
smp'15, Texas, USA, June 2015

Potential theory based simulations of unsteady propeller forces including free surface effects

Martin Greve[1], **Moustafa Abdel-Maksoud**[2]

[1]ThyssenKrupp Marine Systems, Kiel, Germany
[2]Hamburg University of Technology, Hamburg, Germany

ABSTRACT

For several applications, such as offshore supply vessels, the effect of the water surface on the propeller performance cannot be neglected. The calculation of the highly unsteady loads on propellers of offshore supply vessels demands the application of a RANSE-solver. But within a design process these investigations are rarely conducted due to the high complexity and the large computational effort. Therefore less complex numerical tools based on the Potential Theory are mostly used. The results of the numerical investigation are given in terms of propeller thrust and torque fluctuations. The paper reports on a method developed to determine wave loads and free surface effects on free running ship propellers in simulations based on a Boundary Element Method (BEM). This refers to purely non-viscous simulations using a BEM and those using a coupling algorithm to a RANSE-solver. The propeller operates in the vicinity of the free water surface and in some cases ventilates. The dynamic forces acting on the propeller are determined in unsteady manner.

Keywords

BEM, unsteady, free surface, propeller

1 Introduction

Propellers operating near the free water surface can occur, when ships sail with shallow draft, or from large-amplitude ship motions. This happen for instance at offshore supply vessels in transit mode, when they have to keep a specific course or in dynamic positioning mode, when the propulsion unit can have high loading. The propeller then operates in a complex flow field under highly unsteady inflow conditions, dominated by viscous effects. These effects are a combination of wave orbital velocities and ship influence and also separation and ventilation effects can occur at the propeller blades. It is obvious, that most of these flow situations cannot be computed in detail with a potential method, in which viscous effects are neglected.

Different numerical approaches have been develped in the past in order to determine the unsteady loads acting on propellers, which operate under free surface influences. A derivation of integral equations for calculating the circulation distribution on propellers, that partly emerge out of the water, was given by Isay [14] in 1966 based on the lifting line theory. Later, several models based on potential theory were developed, often based on a *BEM*, which was developed by Hess and Smith [12] and later enhanced by Hess [11], who provided the first method using a source and dipole distribution on the surface of a body to model thickness and lift of airfoils. The first *BEM*s for propellers were developed by Hess and Valarezo [13] and by Kerwin et al. [17]. Also methods, in which a free water surface is taken into account, were developed in order to determine the wave-field of ships and ship resistance (see e.g. a linearised steady approach by Dawson [4] and non-linear steady methods by Ni [21] and Jensen [15]). Furthermore, methods were presented e.g. by Young [24] for computing the flow-situation of surface-piercing propellers.

Because most of the viscous effects occurring at propellers operating in the vicinity of a free water surface cannot be captured by potential flow methods and *RANSE* simulations are very expensive, several propeller models were established. These methods can be one-way or two-way coupling models and often the underlying solver is a *RANSE*-solver, in which the propeller is not present. The propeller action is determined externally with either simple algorithms as reported by Carrica et al. [3] or Müller et al. [20], who use a coefficient-based model, or more sopisticated solvers, such as a *BEM* (see e.g. Greve et al. [8]). With the latter kind of propeller models the interaction between the propeller and a hull or thruster housing can be determined. Also three-dimensional effects, such as the propeller slip stream and tip-vortex flows can be captured.

Before *RANSE* solvers became widely available in the late 1990s, more insight was gained from large experimental studies, than from numerical tools. One of the first investigations in the era of controllable pitch propellers was published by Gutsche [9], who investigated the side forces and force fluctuations on a single blade of a propeller operating in oblique inflow conditions in order to investigate the loads acting on the pitch adjusting system. Later, Heinke [10] presented experimental results in terms of stationary and dynamic loads acting on azimuthing podded drives. More recently, numerous experimental campaigns were performed at *MARINTEK* addressing unsteady loads on thruster or pod-propellers. For example, Amini [1] gives results measured at a pod propeller operating in waves; Koushan et al. [18], [19] report on experiments with a thruster having different immersion ratios in waves. The

authors present dynamic propeller forces as well as forces and moments acting on a single blade.

This paper presents a development of potential theory based numerical tools for the determination of loads acting on propellers operating in the vicinity of the free water surface. The free water surface boundary conditions are implemented in an unsteady formulation in the *BEM*. The numerical methods are described in Section 2 followed by validation and verification studies for propeller open water performance and a propeller operating under consideration of wave orbital velocities. The second case combines effects of unsteady load changes and oblique inflow to the propeller. Section 4 presents application cases for the methods. The first refers to a propeller in an open water situation with variing immersion towards the free surface. For this propeller, the time-history of the blade thrust computed with the propeller model for several propeller revolutions is presented and compared to experimental values and *RANSE* simulations. In the second application example, the time-history of blade thrust computed with the *BEM* without considering the free surface boundary conditions, but inheriting wave- and ventilation effects, is compared the measured data.

2 Numerical Methods

The propeller forces are determined based on the potential theory. Therefore, the *BEM* as described in Section 2.1, is used. The possibilities to model the free water surface with panels will be explained, as well as the usage of a wave potential formulation. Both methods can be applied together with a panel split technique, where the panels located above the free surface are not included in the simulation. The second method, which will be briefly discussed, refers to a solver coupling method, in which the *BEM* is used as a propeller model in a *RANSE* simulation. The *RANSE* solver is not explained here.

2.1 Boundary Element Method

The *BEM* refers to a low order Boundary Element Method using flat panels to discretise a body moving in a stationary fluid domain $\mathbb{V}$. The method solves Laplace's equation

$$\nabla^2 \Phi = 0, \tag{1}$$

which gives a complete description of the fluid motion for the velocity potential Φ. The boundary condition on the surface of the body states, that the body must not be penetrated by the fluid and it reads

$$\nabla \Phi \cdot \mathbf{n} = 0, \tag{2}$$

with $\mathbf{n}$ beeing the normal vector of the surface of the body. In far distance of the body, its influence, e.g. the velocity $\nabla \Phi_{ind}$ induced by the body, has to vanish

$$\lim_{r->\infty} \nabla \Phi_{ind} = 0. \tag{3}$$

When applying Equation (2) and using Green's identity, a surface integral formulation of the flow problem can be constructed following Katz and Plotkin [16] and the potential can be determined in any point P located inside the fluid domain

$$\Phi(P) = \frac{1}{4\pi} \int_S \frac{1}{r} \frac{\partial \Phi}{\partial n} - \Phi \frac{\partial}{\partial n} \frac{1}{r} dS, \tag{4}$$

with S beeing the surface of the body. When other potentials are present in $\mathbb{V}$, the total potential can be constructed of several parts because of the linearity of the Laplace equation and it becomes

$$\Phi(P) = \Phi_{ind}(P) - \Phi_M(P) + \Phi_{ext}(P). \tag{5}$$

In Equation (5), the induced potential Φ_{ind} includes the effects of all bodies solved for in the fluid domain on the point P. Φ_M is the motion potential having a negative sign because the problem is set up in a moving frame of reference. The term Φ_{ext} includes all other potentials which can be present in $\mathbb{V}$. This can e.g. be a wave potential or the potential of a free water surface.

In order to determine the two unknowns Φ and $\frac{\partial \Phi}{\partial n}$ in Equation (4), the potential can be expressed in terms of a distribution of sources with source strength σ and doublets with doublet strength μ. The unknowns become

$$\frac{\partial \Phi}{\partial n} = \sigma \quad \text{and} \quad \Phi = \mu. \tag{6}$$

In case a free water surface is taken into account in the simulations, the kinematic and dynamic boundary conditions have to be included on the discretised geometry of the surface. The dynamic boundary condition requires athmospheric pressure at the free surface, is derived from the unsteady Bernoulli equation and is valid at the actual free surface elevation $\zeta = z$. The unsteady dynamic boundary condition reads

$$\begin{aligned} \frac{\partial \Phi_{ind}}{\partial t} = &- \frac{1}{2} \left(\nabla \Phi_{ind} - \mathbf{v}_M + \nabla \Phi_{ext} \right)^2 \\ &+ g\zeta + \frac{1}{2} \left(\mathbf{v}_M \right)^2 + \frac{\partial \Phi_{ext}}{\partial t}. \end{aligned} \tag{7}$$

In Equation (7), the motion velocity $\mathbf{v}_M$ is negative because the equation is set up in the bodies moving frame of reference. The kinematic boundary condition requires the free water surface to move according to the velocity at the surface. The formulation reads

$$\frac{\partial \zeta}{\partial t} = - \frac{\partial \Phi_{ind} + \Phi_{ext}}{\partial z} + \left(\nabla \Phi_{ind} - \mathbf{v}_M + \nabla \Phi_{ext} \right) \cdot \nabla \zeta. \tag{8}$$

The kinematic boundary condition is linearised, the free surface is only deformed in the global vertical direction z.

When a wave potential is used, the potential Φ_{Wave} can be included. This is treated as external potential following Equation (5). The implemented wave potential describes a regular, long crested deep water wave with a wave period T_w, a wave length $L_w = \frac{2\pi}{\omega}$ and a wave height H_w,

according to the linear wave theory. It reads

$$\Phi_{Wave}(x,y,z,\gamma,t) = \frac{H_w g T_w}{4\pi} e^{kz} \cos\left[\omega t - k(x\cos(\gamma) + y\sin(\gamma))\right]. \quad (9)$$

Here, $k = \frac{2\pi}{L_w}$ is the wave number and γ the global travel direction of the wave. A natural, irregular seaway can be constructed from an energy wave spectrum by superposing waves with different lengths, amplitudes, periods, propagation directions and phase shifts.

When a free water surface and/or the wave potential is used, parts of a body can emerge out of the water and hence leave the flow domain $\mathbb{V}$. In this case, a panel split technique is used, which determines the immersion of each panel and modifies its influence factors in the system of linear equations. When a panel is partly immersed, its diagonal matrix element is divided by an immersion factor f_S, as proposed by Söding [22]. The factor f_S is 1 for a completely immersed panel and 0, when completely out of the water.

When the potential in every collocation point on the bounding surfaces of the flow domain is determined, the pressure can be calculated using the Bernoulli equation. Using the local panel area and the normal, the pressure force can be calculated and integrated on the body. For a more detailed description of the numerical method, see [7].

2.2 Propeller model

The propeller model used here is in detail described in [8], where a validation and an application example is given. Because of the advanced propeller modeling and the coupling of two 3-D flow solvers, the method also refers to a solver coupling method. In general, three different coupling modes, referring to an explicit, a semi-implicit and an implicit mode, are implemented. The following description and the simulations shown later are based on the explicit mode. In order to start the coupled simulation, a fully converged solution of the sub-problem is required in each solver, the *BEM* as described above and the *RANSE* solver.

The solver coupling method is based on the exchange of two properties, namely the wake velocity distribution in front of the propeller and force-field of the propeller. These vector fields are exchanged in each time step of the solution process and is determined at 0.5 to 1.0 times the propeller radius in front of the propeller position on a pre-defined grid. Because the *BEM* simulation requires an input of the effective wake field, the propeller induced velocities have to be subtracted from the total wake field beforehand. This is done based on the induced velocities computed with the *BEM*. With this method the axial, radial and tangential velocity components of the wake field are taken into account. One time step with the fully modeled propeller is then conducted in the *BEM* in order to determine the forces. The resulting force distribution is based on the inflow velocity of the last time step in the explit case.

The propeller forces are transferred to the *RANSE* solver and applied as body forces in the fluid domain using a force conservative distribution sceme described by Brunswig et al. [2]. Because the position is also transferred, a three-dimensional representation of the propeller including the force distribution on the pressure side and the suction side is present in the *RANSE* domain. Hence, the propeller lift and (partly) displacement effects including the main flow phenomena, such as the vortices at the hub and the tip and the trailing wake sheet, are represented in the resulting flow field. The time step and the coupling loop ends with the solution of the flow field in the *RANSE* solver.

For including a free water surface in a simulation using the solver coupling method, a transfer based on a Fourier series representation of the surface position is developed in order to pass the position from the *RANSE* solver to the *BEM*. This is required to correctly determine the free surface influence inside the *BEM* with the elevation determined in the *RANSE* solver. A Fourier series for prescribed longitudinal strips of the free water surface is constructed in the *RANSE* solver based on the results of the *Volume of Fluid* model. Only the Fourier coefficients are passed to the *BEM*, where the surface is reconstructed and modeled as rigid wall, where the kinematic free surface boundary condition is solved. The resulting algorithm is fast and robust.

3 Validation and Verification

This section reports on a verification study showing the grid dependency of propeller open water simulations using the *BEM*. This is followed by a validation of one of the methods implemented in order to compute the thrust forces acting on a single blade of a propeller operating in waves without emerging out of the water. The propeller investigated in the following refers to a four-bladed controllable pitch truster-propeller. The simulations are conducted for the design pitch setting $P/D = 1.2$ only.

3.1 Propeller open water performance

In order to determine the grid dependency of the simulation results, seven different grids are investigated. One propeller blade is discretised with between 8 and 32 panels in radial direction and between 12 and 48 panels in tangential direction (combined number on both sides of the blade). The resulting grids have between 96 and 1536 panels per blade and the grid study is conducted at an advance ratio of $J = 0.9$. One exemplary propeller blade grid with 28x42 panels is displayed in Figure 1. With increased grid density, the simulation time rises in an approximate quadratic manner with respect to the panel number.

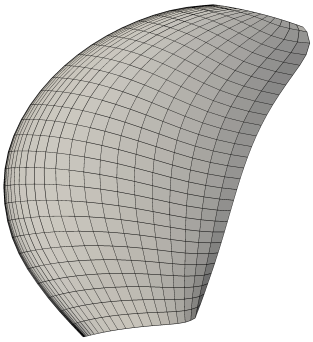

Figure 1: Exemplary grid of one propeller blade with 28 panels in radial and 42 panels in tangential direction

For displaying the results in Figure 2, Figure 3 and Figure 4, the K_T and K_Q-values computed with the *BEM* in the grid study are non-dimensionalised by the value of the finest grid solution. The blade grid study displayed in Figure 2 shows a good convergence behaviour towards the finest grid solution. This result depends on the refinement function used and can differ for different propeller geometries. The result of the grid with 864 panels (24x36) shows a difference to the finest grid solution of about 1.0%. The deviation to the solution of the finest grid is smaller for the propeller thrust than for the torque.

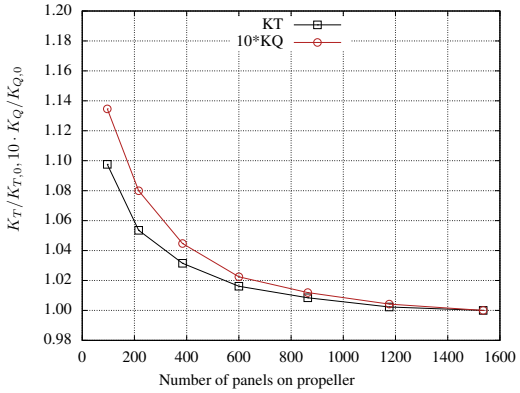

Figure 2: Influence of blade grid discretisation on the computed thrust and torque coefficients

When investigating the influence of the trailing wake sheet aft of the propeller blade in Figure 3, it can be seen that the length of this sheet is an important parameter. The velocities induced from the wake panels on the blade panels reduce the blade forces, resulting in a strong influence of the wake length, when modeled for less than two propeller rotations. Above this value, the influence is below 1.0% to the solution of the finest grid. For further investigations, the wake length referring to 480° of a propeller rotation is selected, showing an error of approx. 1.0% compared to the longest wake representation. In order to account for the wake influence, the trailing wake sheet does not necessarily have to be physically modelled by panels. A far field influence, as e.g. discussed by Greco et al. [6] could be taken into account for a more realistic model and reduce simulation costs.

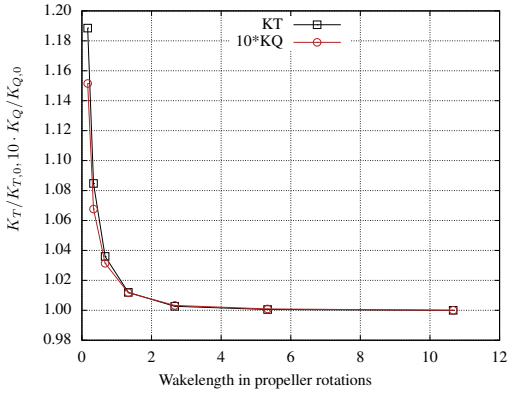

Figure 3: Influence of length of discretised wake sheet on the computed thrust and torque coefficients

An investigation of the influence of a different iteration step size on the result quality is given in Figure 4. This is mainly important because the iteration step size determines the length of the wake panels, also in a steady simulation. A large iteration step size results in long wake panels, which usually have a large aspect ratio. With this panels, the deformation and - in particular - a smooth roll-up of the tip vortex cannot be captured and often a poor convergence behaviour of the wake position results. Hence, the forces computed at the blade also fluctuate. When the iteration step size is smaller, the discretised geometry of the deformed wake sheet is more smooth and the wake roll-up can be better represented by the panels. Because the deformation of wake panels is expensive, the simulation time increases drastically with a fine representation of the wake sheet. A good compromise can be found for an iteration step size referring to 6° of a propeller rotation showing an error of approx. 1% to the solution of the finest grid in Figure 4. This investigation also holds for unsteady simulations, as the time step size determines the size of the wake panels in the same way, as the iteration step size in steady simulations.

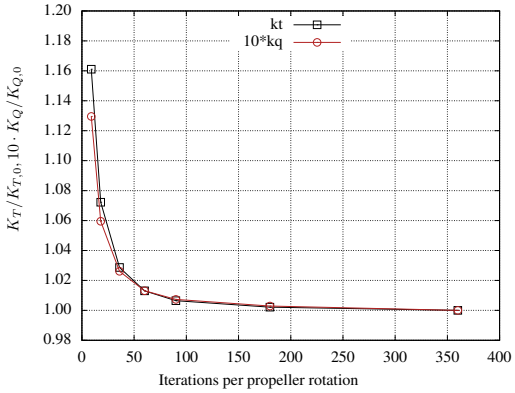

Figure 4: Influence of iteration step size on the computed thrust and torque coefficients

The input parameters chosen based on the grid studies are summarised in Table 1. These values result in open water thrust and torque coefficients close to the values measured in the towing tank for the model scale propeller.

Parameter	Value
Blade grid size	28 x 42 panels
Iteration step size	6° of one propeller rotation
Length of trailing wake	480° of one propeller rotation

Table 1: Simulation parameters obtained from Propeller A grid study

3.2 Propeller forces under consideration of a wave potential

In this validation example, the *BEM* is used together with a wave potential formulation, as described in Section 2. This section shall demonstrate the ability of the method to compute unsteady propeller forces under wave influence without an interaction with the free water surface. The simulations refer to a fully modelled propeller in an open water setup, but only shallowly immersed. The propeller is operating under a regular head wave. Several experimental results were made available by *MARINTEK* and a larger investigation is given in [7]. Here, the results for one steady propeller immersion and one wave length is presented. The propeller diameter is $200mm$, the steady immersion of the propeller center towards the undeformed free surface is $250mm$, the wave height is $260mm$ and the wave period is $1.5s$. The unsteady single blade thrust forces are made non-dimensional by the values for the deeply immersed propeller and are presented and compared to the experimental results in the figures 5, 6 and 7.

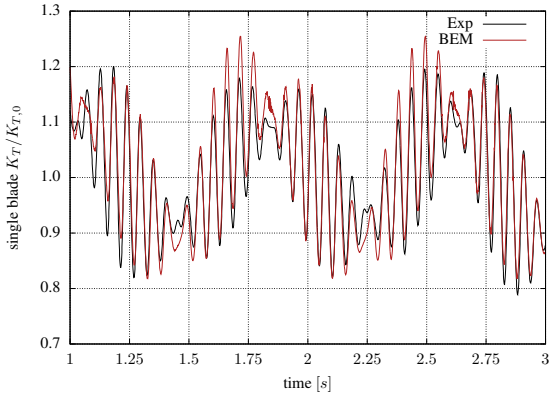

Figure 5: Blade thrust in regular head wave at $J = 0.6$

The non-dimensional single blade thrust coefficient at $J = 0.6$ for the propeller under the wave is shown in Figure 5. Two main frequencies can be found in the unsteady forces. The first, higher frequency, is a results of the vertical fraction of the wave orbital velocities and refers to the blade frequency, at which the blade passes the non-uniform velocity field. When the orbital velocities are directed upwards, the blade load is higher in the first half of the rotation (descending blade) and lower in the second half (ascending blade). In case of a wave crest or trough, the vertical fraction of orbital velocities is zero and the blade frequency fluctuations also reduce for about two propeller revolutions. This can be seen in Figure 5 at $1.4s$ for a wave crest, where the loading of the blade is minimal, and at $1.8s$ for a wave trough, where the blade loading is maximal. The second, lower frequency, which can be seen in Figure 5, is the encounter frequency between the propeller and the wave and results from the horizontal fraction of the orbital velocities. They result in a different advance velocity towards the propeller and shift the blade loading. The simulation results shown with the red curve are in good agreement towards the experimental. Both described frequencies can be captured well and also the amplitudes are well predicted with the *BEM*, showing only small overshoots shorty before the wave trough, when the calculated blade loads are higher, than the measured. The thrust fluctuates with an amplitude of approx. 20% around the medium value $K_{T,0}(J = 0.6) = 0.0862$.

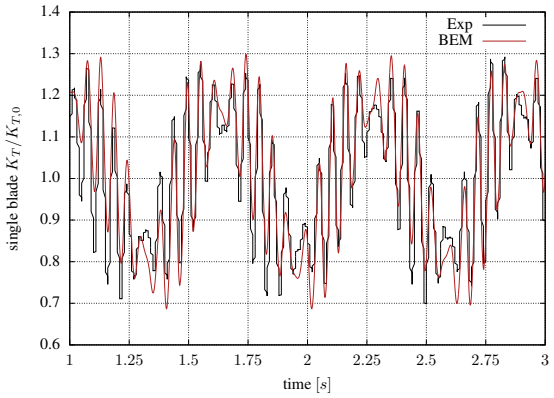

Figure 6: Blade thrust in regular head wave at $J = 0.9$

The single blade thrust fluctuations at an advance ratio of $J = 0.9$ are shown in Figure 6. The non-smooth representation of the measured results is a possible cause of the low-pass signal filtering. Again, the differences between the numerical and the experimental results are small. Both the small scale and the large scale fluctuations are larger, than at $J = 0.6$. The amplitude of thrust fluctuations is approx. $30 - 50\%$ around the medium value $K_{T,0}(J = 0.9) = 0.0574$. For the lowest loading, the agreement between simulation and experiment becomes slightly worse whereas the overall behaviour is still captured well. The absolute thrust is only 25% of the value at $J = 0.6$, the thrust fluctuates with approx. $100 - 150\%$ aroung the medium value $K_{T,0}(J = 1.2) = 0.0222$.

Although the clearance between blade tip and water surface is only $20mm$ in case of a wave trough in the presented case, the free surface influence is small and the results of the *BEM* show a good congruence to the measured values. This becomes worse for larger propeller thrust loading or a smaller immersion of the propeller hub. One interesting finding is, that the absolute value of thrust fluctuation is

about the same for the three investigated advance ratios.

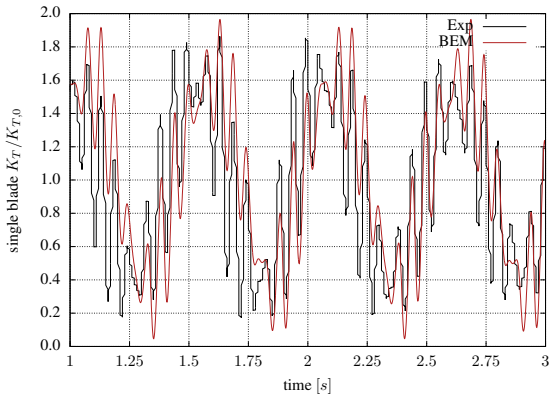

Figure 7: Blade thrust in regular head wave at $J = 1.2$

4 Applications

This section reports on two application studies of the developed numerical methods for propellers operating under free surface influence. The first refers to a propeller in an open water situation subjected to a shallow immersion. The single blade thrust forces are simulated with the propeller model and compared to *RANSE* results by Wöckner-Kluwe [23] and to measured forces. A comparison is presented for three different immersion ratios of the propeller hub, $H/R = 1.5$, $H/R = 1.0$ and $H/R = 0.0$, with the immersion of the hub H and the propeller radius R. The second study is similar to the one given in Section 3.2, but with a more pronounced influence of the free water surface. The unsteady blade loads computed with the wave potential method and using the panel split technique are presented and compared to measured data.

4.1 Propeller with variing immersion

When the propeller operates with a shallow immersion, both ventilation and cavitation can occur. The first because the propeller sucks air into the water and can sometimes keep a massive amount of air around it for several revolutions. The second because the hydrostatic pressure is low resulting in an earlier cavitation inception. Both phenomena are even more pronounced, when the propeller operates under high loading, which is the case for a ship in heavy seas or in dynamic positioning mode. Because the described effects are driven by viscosity, they are unlikely to be determined with a potential-based numerical method. Furthermore, they often appear stochastically, so they are even difficult to reproduce in experiments. So, the aim of this study is not to exactly reproduce the measured thrust values, but more to capture the maximum load fluctuations in order to be able to predict the structural loads on the propulsor and its components.

The results are given in Figure 8. The first investigated immersion ratio is $H/R = 1.5$, presented in Figure 8a and Figure 8b. In this case, the clearance between the blade tip and the undisturbed free surface is $0.5R$. At an advance ratio of $J = 0.6$, no pronounced free surface influences can be found in the blade forces given in Figure 8a. In this case, also simulations including a panelling and a solution of the free water surface boundary conditions inside the *BEM* are given (red triangles). The results of the numerical methods are in line with the experimental results showing a slight decrease of blade thrust in the first half of the revolution and a slight increase in the second half. In the case, where the free surface is modeled in the *BEM*, the forces are already smaller for the blade in the topmost position referring to $0°$ denoting an overprediction of the interaction between the water surface and the blade.

For the higher blade loading at $J = 0.3$, shown in Figure 8b, the experimental results do not show a constant trend. The propeller strongly ventilates in most of the revolutions, resulting in only 30% of $K_{T,0}$, but does not ventilate in others. All measured curves are more or less horizontal, so the ventilated air content is kept in the water for the complete propeller rotation. This acts like a lowered water density and a high air content around the propeller was found in the experiments. This behaviour could not be reproduced with any of the computational methods. The *RANSE* results do not show pronounced ventilation effects and only the blade tip emerges out of the water near the topmost position. In the results computed with the propeller model (green crosses), the measured range of thrust deviations can nearly be captured, but in contrast to the experimental results, within a single revolution, when a thrust breakdown up to $0.4K_{T,0}$ occurs around the topmost position for a short period of time.

In the figures 8c and 8d, a smaller hub immersion of $H/R = 1.0$ is investigated and again, large differences between simulation and experimental results occur. The results of the *RANSE* method and the propeller model are in a satisfying agreement, showing an emerging of the blade at the same blade angle. The thrust breakdown is larger for the propeller model. The results of the measurements are again horizontal at between 30% to $40\%K_{T,0}$ for all propeller revolutions in the presented period of time. The minimum value of measured thrust can be reproduced by the propeller model, which also accounts for the higher blade loading shown in Figure 8d, where only 10% to $20\%K_{T,0}$ are left. In this case, a pronounced wave trough occurs above the propeller position in the simulation results and nearly the complete blade emerges, when beeing around $0°$. In the *RANSE* results, a hose of air developes, which can be sustained in the water for parts of the revolution.

When the propeller hub is at the height of the undisturbed free surface, the videos taken during the experimental investigation show a large amount of small bubbles in the water around the propeller. The thrust breaks down to zero for all of the results shown in the figures 8e and 8f, when the blade is in the upper half of the revolution. Again, the ventilation observed in the experiments cannot be reproduced by the methods used here, but for the *RANSE* method at $J = 0.3$, where more pronounced ventilation effects occur and the computed forces are closer to the measured curves.

Wave Code	Static Propeller Immersion $[mm]$	Wave Height $[mm]$	Wave Period $[s]$
8242	250	300	2.0
8211	100	100	1.5
8221	100	200	1.5

Table 2: Overwiev of simulation cases for propeller in regular wave

4.2 Propeller with variing immersion under wave influence

In the case of a propeller operating in waves, several propeller revolutions have to be simulated in order to capture a full encounter period. This is because the discrepancy between the high rate of propeller revoultion of $18rps$ and the quite large wave period. For this situation, the *BEM* - as a fast computation method - in combination with the above described wave potential is used. The results are shown in Figure 9 for a time-period of $2s$. The unsteady single blade thrust forces are determined for the advance ratios $J = 0.6$ and $J = 0.9$ and three different waves, as shown in Table 2.

In the first case (wave code 8242) shown in the figures 9a and 9b, the propeller immersion is $H/R = 2.5$ and the free surface influence is small. The amplitude of thrust fluctuations can be reproduced well by the simulations, whereas the agreement is better for the higher thrust loading at $J = 0.6$. At $J = 0.9$, the calculated thrust is slightly higher, when the propeller is under a wave flank in a crest to trough situation, whereas it is lower in a trough to crest situation. When the propeller is located under a wave crest or a trough, the agreement between experiment and simulation is satisfactory.

The results of the second investigation (wave code 8211) are shown in figures 9c and 9d. The propeller immersion is lower, so that the clearance between the blade in the topmost position and the undisturbed free surface is zero. When looking at the results for $J = 0.6$, a large discrepancy between the measured and calculated results can be seen. In the *BEM* simulations, the blade only emerges out of the water in the upper half of the rotation, when situated in a wave trough. When under a wave crest, the thrust fluctuates around $K_{T,0}$. In the experimental results, the measured thrust coefficient is below $0.4K_{T,0}$ for the complete time-series denoting a massive air drawing by the propeller in the wave trough phase. This is not the case for the advance ratio $J = 0.9$ depicted in Figure 9d. Here, the congruence between the curves is better and similar positions between wave and propeller lead to a blade emergence. The amplitude of thrust fluctuations for the ventilating propeller computed by the *BEM* is larger, showing overshoots with negative thrust values. The experimental results show amplitudes of $1.05K_{T,0}$ with values between $0.15K_{T,0}$ and $1.20K_{T,0}$

The third case with wave code 8221 is similar to wave 8211 with twice the wave amplitude. When comparing the results for $J = 0.6$, the time-instant at which ventilation occurs and also the non-ventilating thrust fluctuations are in a good agreement. In both results, the thrust is zero for the blade in the topmost position in the wave trough phase. After passing of the wave trough, the air drawing of the propeller lasts for two revolutions longer in the experiments. This behaviour can not be reproduced in the simulations because of the simple approach. At $J = 0.9$, the agreement is slightly worse with higher values for the non-ventilating propeller and partial overshoot of the *BEM* results in both directions.

5 Conclusion

In the paper potential theory based methods for computing unsteady forces for propellers operating near the free water surface are presented and a validation and verification study showing the general applicability is given in Section 3. The first application study in Section 4.1 is devoted to a shallowly immersed propeller in waves and results are presented for the *BEM* with modeled free water surface and the propeller model compared to *RANSE* results and experimental values. The solution of free water surface boundary conditions in the *BEM* for a propeller is only working for specific cases. When the interaction is too large, the simulations do not converge because the free surface boundary conditions resulting in extreme deformations. This method seems more appropriate for computing wave resistance of other submerged bodies or ships. An application of the developed algorithm for ships and an immersed spheroid is given by Goettsche [5].

The simulations using the propeller model show good results, when compared to the *RANSE* results and the curves for the blade thrust are in good agreement. However, the dynamics of the process in model scale, where the air content stays around the propeller for many rotations seem to be difficult to reproduce. The maximum thrust breakdown can be prediced well with the propeller model, so it could be used for the determination of load fluctuations on ventilating propellers.

In Section 4.2, an application of the method for shallowly immersed propellers operating in waves is presented. The results are encouraging and for most of the cases a good agreement between the simulation results and the experimental results is found. The experimental results are not in any case reasonable, e.g. when comparing Figure 9c and Figure 9e, where the propeller fully ventilates when subjected to a lower wave, whereas it only ventilated part-time

for a higher wave.

Future work could be related to improving the robustness of the numerical implementation of the free water surface boundary conditions in the *BEM*. A possible approach is a numerical damping of the free surface elevation or a prescribed elevation pattern based on the surrounding surface area, when the elevation of panel edges is too high or low. Also the overshoot behaviour of the *BEM* in simulations with the wave potential could be improved. Here overshoots occur both, when the blade emerges completely out of the water and when it re-enters. This is somehow related to the influence of the trailing wake an none of the numerical technics tested seemed to solve the problem.

6 Acknowledgements

The work has been performed under the aegis of ProSee, a sub-project of the joint European co-laborative Era-Net MARTEC project PROPSEAS. The project was sponsored by the German Federal Ministry for Economic Affairs and Energy.

REFERENCES

[1] H. Amini. Azimuth propulsors in off-design conditions. PhD thesis, Norwegian University of Science and Technology, Department of Marine Technology, 2011.

[2] J. Brunswig, M. Manzke, and T. Rung. Explicit and Implicit Coupling Strategies for Overset Grids. In Proceedings of the 10th Symposium on Overset Composite Grids and Solution Strategies, 2010.

[3] P.M. Carrica, K.-J. Paik, H.S. Hosseini, and F. Stern. URANS analysis of a broaching event in irregular quartering seas. Journal of Marine Science and Technology, (13):395–407, 2008.

[4] C. W. Dawson. A Practical Computer Method for Solving Ship-Wave Problems. In Proceedings of 2nd Conference on Numerical Ship Hydrodynamics, 1977.

[5] U. Göttsche. Implementierung der instationären Randbedingung an der freien Wasseroberfläche in einem Randelementverfahren. Master's thesis, Hamburg University of Technology, 2014. In German.

[6] L. Greco, F. Salvatore, and F. Di Felice. Validation of a Quasi-potential Flow Model for the Analysis of Marine Propellers Wake. In Proceedings of the 25th Symposium on Naval Hydrodynamics, 2004.

[7] M. Greve. Non-viscous calculation of propeller forces under consideration of free surface effects. PhD thesis, Hamburg University of Technology, 2015. thesis submitted.

[8] M. Greve, K. Wöckner-Kluwe, M Abdel-Maksoud, and T. Rung. Viscous-Inviscid Coupling Methods for Advanced Marine Propeller Applications. International Journal of Rotating Machinery, 2012.

[9] F. Gutsche. Untersuchung von Schiffsschrauben in schräger Anströmung. Schiffbauforschung, 3:97–122, 1964. In German.

[10] H. J. Heinke. Investigation about the forces and moments at podded drives. In Proceedings of the First International Conference on Technological Advances in Podded Propulsion, Newcastle University, UK, pages 305–320, 2004.

[11] J. L. Hess. Calculation of Potential Flow About Arbitrary Three-Dimensional Lifting Bodies. Technical report, Douglas Aircraft Division, Long Beach, California, 1972.

[12] J. L. Hess and A. M. O. Smith. Calculation of Non-Lifting Potential Flow about arbitrary Three-Dimensional Bodies. Technical report, Douglas Aircraft Division, Long Beach, California, 1962.

[13] J. L. Hess and W. O. Valarezo. Calculation of Steady Flow About Propellers by Means of a Surface Panel Method. In Proceedings of AIAA 23rd Aerospace Sciences Meeting, 1985.

[14] W. H. Isay. Zur Theorie des Propellers mit aus dem Wasser herausschlagenden Flügeln. 1966. In German.

[15] G. Jensen. Berechnung der stationären Potentialströmung um ein Schiff unter Berücksichtigung der nichtlinearen Randbedingungen an der Wasseroberfläche. Schriftenreihe Schiffbau, No. 484, 1988. In German.

[16] J. Katz and A. Plotkin. Low-Speed Aerodynamics. Cambridge University Press, 2001.

[17] J. E. Kerwin, S. A. Kinnas, J.-T. Lee, and W.-Z. Shih. A Surface Panel Method for the Hydrodynamic Analysis of Ducted Propellers. SNAME Transactions, 95:93–122, 1987.

[18] K. Koushan, S. J. B. Spence, and T. Hamstad. Experimental Investigation of the Effect of Waves and Ventilation on Thruster Loadings. In Proceedings of the First International Symposium on Marine Propulsors, 2009.

[19] K. Koushan, S. J. B. Spence, and L. Savio. Ventilated Propeller Blade Loadings and Spindle Moment of a Thruster in Calm Water and Waves. In Proceedings of the Second International Symposium on Marine Propulsors, 2011.

[20] S.-B. Müller, M. Steden, J. Neugebauer, M-F. El-Haddad, and M. Abdel-Maksoud. Comparing a Propeller Model with a Rotating Propeller in an CFD-simulation of the Viscous Flow around a Ship. Technical report, Institute of Ship Technology and Transport Systems, University of Duisburg-Essen, 2006.

[21] S.-Y. Ni. Higher-order panel methods for potential flows with linear or nonlinear free-surface boundary conditions. PhD thesis, Chalmers University of Technology, 1987.

[22] H. Söding. Towards Fully Non-Linear Floating Body Simulations by a Potential Method. In Proceedings of the 31st International Conference on Ocean, Offshore and Arctic Engineering, 2012.

[23] K. Wöckner-Kluwe. Evaluation of the unsteady propeller performance behind ships in waves. PhD thesis, Hamburg University of Technology, 2012.

[24] Y. L. Young. Numerical Modeling of Supercavitating and Surface-Piercing Propellers. PhD thesis, The University of Texas at Austin, 2002.

DISCUSSION

Question from Rickard Bensow

How did you determine the free surface in the *BEM* from the *RANS* and did you make any sensitivity analysis of this choice? (As the free surface is not apparent in a mixture flow.)

Authors' Closure

The free surface is determined by the volume of fluid model in the RANS-part of the simulation. The height coordinates of the free surface are determined by interpolating the exact position in the volumetric cells, at which the mixture fraction is 0.5. This is done for user-defined points which are specified during the setup of the simulation on an orthogonal grid on the undisturbed free surface. Therefore the part of the free surface passed to the *BEM* can be significantly smaller than the *RANS* domain so the computational effort of the *BEM*-part is reduced. For prescribed lengthwise sections (in main flow direction) on this grid fourier series representations of the free surface are calculated by

$$h(P) = \frac{h_0}{2} + \sum_{k=1}^{n} \left[A_k cos(k\frac{2\pi}{L}P_0) + B_k sin(k\frac{2\pi}{L}P_0) \right].$$

Here, $\frac{h_0}{2}$ is the mean value of free surface elevation, L is the total length of the Fourier series in longitudinal direction and P_0 is the actual position in the range between zero and L. Each lengthwise Fourier series is constructed using n discrete height values $h(P)$ in longitudinal direction and the Fourier coefficients A_k and B_k.

The advantage of using Fourier series is the avoiding of reproducing local deformations of the free surface. Only the larger-scale deformations shall be passed to the *BEM* simulation when re-constructing the free surface. At the discretised free surface the kinematic boundary condition is solved. The number of coefficients n is chosen in order to get a smooth representation of the free water surface in the *BEM*.

Question from Sverre Steen

What do you think is the reason for the systematic underprediction of ventilation extent and thrust loss in partial ventilation? What physical effects aren't properly represented in the calculations?

Authors' Closure

The question refers to the *RANSE* part of the simulations, because the free surface position is determined in the *VoF* model of the *RANS*-part of the simulations given in Chapter 4. In the simulations the amount of air or mixture flow sucked downwards by the propeller is significantly lower than in the experiments. This was confirmed by images and videos kindly provided by *MARINTEK*. Possible reasons for that could be the surface sharpening used in the *VoF* model or unsufficient grid resolution.

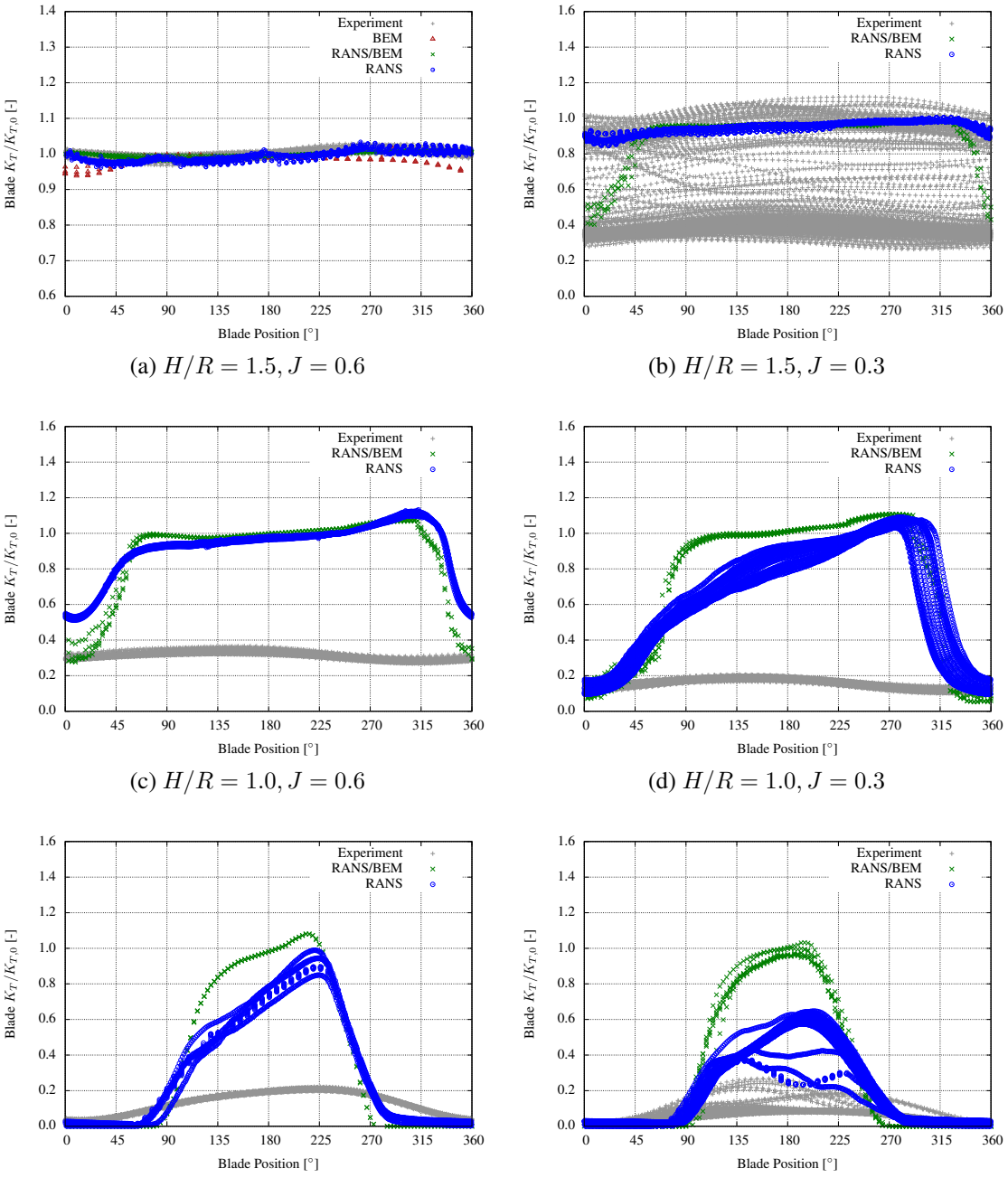

(a) $H/R = 1.5, J = 0.6$

(b) $H/R = 1.5, J = 0.3$

(c) $H/R = 1.0, J = 0.6$

(d) $H/R = 1.0, J = 0.3$

(e) $H/R = 0.0, J = 0.6$

(f) $H/R = 0.0, J = 0.3$

Figure 8: Comparison of single blade thrust coefficients between the results of the propeller model, *RANSE* results by Wöckner-Kluwe [23] and measured values for the free running propeller in calm water. The unsteady thrust coefficient K_T for the shallowly immersed propeller is normalised by the value $K_{T,0}$ for the deeply immersed propeller. The immersion of the propeller center is H, the propeller radius is R.

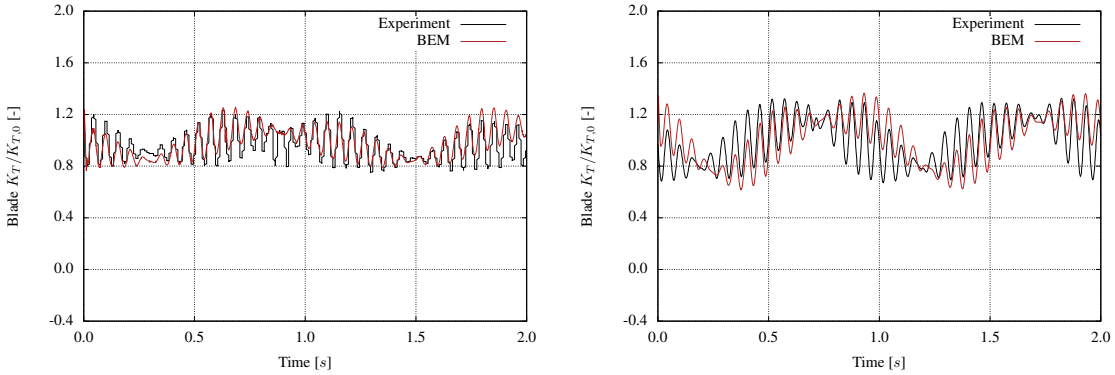

(a) Wave 8242, $J = 0.6$

(b) Wave 8242, $J = 0.9$

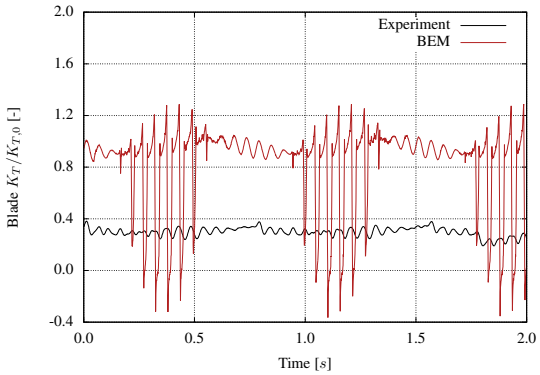

(c) Wave 8211, $J = 0.6$

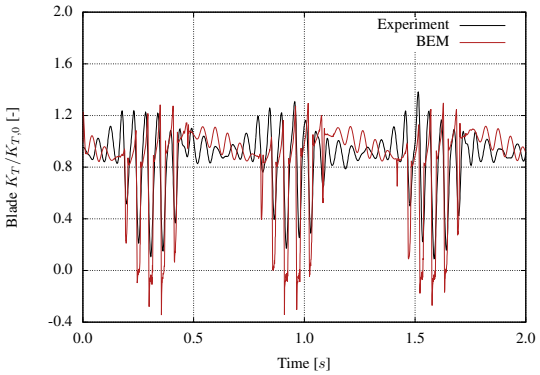

(d) Wave 8211, $J = 0.9$

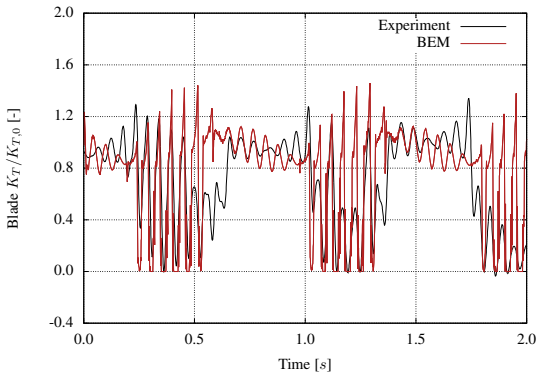

(e) Wave 8221, $J = 0.6$

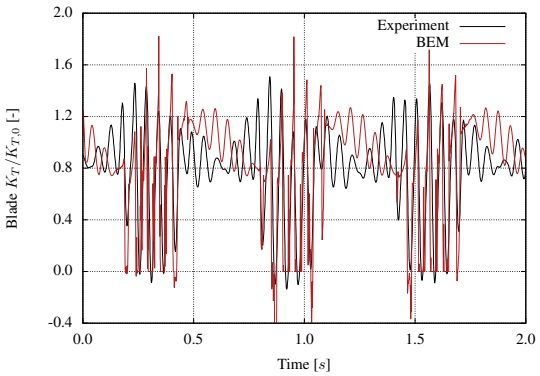

(f) Wave 8221, $J = 0.9$

Figure 9: Comparison of single blade thrust coefficients between the results of the *BEM* and the measures values for the free running propeller in regular waves. The wave height is H_W, the wave period is T_W.